

SELF-CONSISTENT MODELS FOR THE X-RAY EMISSION FROM SUPERNOVA REMNANTS: AN APPLICATION TO KEPLER'S REMNANT

JOHN P. HUGHES AND DAVID J. HELFAND¹
 Columbia Astrophysics Laboratory, Columbia University
 Received 1984 July 9; accepted 1984 October 31

ABSTRACT

We have developed a novel solution to the problem of time-dependent ionization in a shock-heated plasma and have incorporated it into a standard, spherically symmetric hydrodynamic shock code to study the evolution of supernova remnants (SNRs). Our approach to the ionization calculation is to use the eigenvalue method of solution for the matrix formed from the coupled system of rate equations expressing the time development of the ionization structure. Combined with the numerical shock code which enables us to examine emission both from the ambient interstellar gas heated by the outward-moving blast wave and from the supernova (SN) ejecta as it encounters the reverse shock propagating inwards, this model serves as a powerful tool in understanding the X-ray emission from young SNRs.

As a first application, we have fitted all the available observations of Kepler's SNR obtained with the imaging and spectral instruments of the *Einstein Observatory*. We find that there are two classes of models which adequately describe the data. If the remnant is in the Sedov phase, most of the observed X-rays come from the shocked interstellar medium, and we require near-solar abundances, a high interstellar-medium density in the vicinity of the remnant ($\geq 6 \text{ cm}^{-3}$), and an upper limit to the SN ejected mass of $0.2 M_{\odot}$. A somewhat better fit is possible, however, if most of the emission arises from the shocked ejecta (the intermediate case of emission from both components is excluded by the data). In this case, we require significant heavy-element overabundances and an ejected mass of $\sim 4 M_{\odot}$. This case also requires a rather large ambient density ($\sim 2 \text{ cm}^{-3}$), although this can easily be supplied by the pre-SN wind of the progenitor star. In either case, an initial mass for this star of $\geq 7 M_{\odot}$ is indicated. We discuss the implications of this result, concluding that it is neither statistically improbable nor physically unreasonable; if correct, it requires that at least some Type I SNs originate from intermediate mass stars. Tests which could strengthen this conclusion and allow a choice between the two evolutionary scenarios are proposed.

Subject headings: hydrodynamics — nebulae: individual — nebulae: supernova remnants — shock waves

I. INTRODUCTION

X-ray emission from young supernova remnants (SNRs) provides the most direct measure of the manner in which the gravitational energy in a supernova (SN) core collapse couples to the surrounding medium. Recently, observations using the *Einstein Observatory* (Giacconi *et al.* 1979) have revealed the complicated nature of both the X-ray spectra and spatial morphology of these remnants in the Galaxy (Becker *et al.* 1979, 1980a, b, c; Murray *et al.* 1979; Pye *et al.* 1981; Reid, Becker, and Long 1982; Seward, Gorenstein, and Tucker 1983; White and Long 1983; Pisarski, Helfand, and Kahn 1984) and in the nearby Magellanic Clouds (Mathewson *et al.* 1983). It has long been known that the X-ray emission from these objects arises from a high-temperature plasma (primarily interstellar gas) which has been heated by the passage of a rapidly moving shock front. However, a realistic model for the emission must include such factors as the time dependence of the ionization state of the hot matter, the presence of supernova ejecta enriched in heavy elements, the amount of mixing between this ejecta and the shocked interstellar matter, the rate of equilibration of the electron and ion temperatures behind the shock, density inhomogeneities in the ambient medium, etc. Considering the substantial disagreement between the new data and the standard shock models which ignore these effects (see, e.g., Danziger and Gorenstein 1983), it now seems appropriate to

include such features in modeling remnant evolution. We present here an SNR model which involves the calculation of the nonequilibrium ionization (NEI) structure throughout the interior of a remnant and which, since it is based on a numerical hydrodynamic shock code, can examine the X-ray emission from the supernova ejecta as well as from the heated ambient medium.

Most previous studies involving NEI (Hamilton, Sarazin, and Chevalier 1983; Shull 1982; Gronenschild and Mewe 1982) have considered only those astrophysical situations in which the analytic expressions for temperature and density of Sedov (1959) are applicable. Comparison with observed SNRs is then limited to cases in which the expanding SN shock has swept up much more ambient material than was ejected in the explosion, and where emission from the ejecta is ignored. Until now, there has been only one published example of a model including NEI and utilizing a numerical calculation for the hydrodynamics (Itoh 1977); this model was compared to pre-*Einstein* observations of the remnant Cas A and, thus, was only weakly constrained by the data. Models such as we present here are expected to be more realistic in describing young remnants because they include the X-ray emission from the supernova ejecta. During the early expansion of a remnant, this matter is heated to X-ray temperatures by the passage of a reverse shock (McKee 1974; Gull 1975b) which arises from the deceleration of the ejecta by the ambient interstellar medium (ISM). For certain choices of the model parameters, this emis-

¹ Alfred P. Sloan Research Fellow.

sion can be the dominant source of X-ray flux, while in many other cases it contributes significantly to the surface brightness profile. In this paper we apply our NEI hydrodynamic-shock model to observations of the remnant of Kepler's SN (SN 1604), one of the youngest known SNRs in the Galaxy and presumably one for which these effects should be prominent.

We have employed a different approach from all previous NEI studies for solving the coupled differential equations expressing the time development of the ionization structure. We begin by writing the system in matrix form and considering it as an eigenvalue problem which then can be solved once and used repeatedly in all the numerical models. We discuss the details of our solution as well as those of the hydrodynamic shock code in § II; further information on the matrix approach is found in the Appendix. In § III, we derive the constraints which can be applied to the parameter space available to the model simply from considering the size, age, and total X-ray flux of Kepler's SNR. In § IV we present comparisons between our model and the observations, where we fit, in a self-consistent manner, both the imaging and spectral data on Kepler collected with the instruments on board the *Einstein Observatory*. The final section discusses the implications of our results, summarizes our conclusions, and presents some directions for future research.

II. SNR MODEL

a) Nonequilibrium Ionization: A Matrix Approach

The basic equation of our NEI calculation is

$$\frac{dF_i}{dt} = n_e \{ \alpha_{i-1}(T) F_{i-1} - [\alpha_i(T) + R_{i-1}(T)] F_i + R_i(T) F_{i+1} \}, \quad (1)$$

where F_i is the fraction of a given atomic species in the i th ionization state ($i = 1$, neutral; $i = 2$, singly ionized; etc.), n_e is the number density of electrons, $\alpha_i(T)$ is the ionization rate by electron collision from state i (into state $i + 1$), and $R_i(T)$ is the recombination rate (including both radiative and dielectronic processes) to state i (from state $i + 1$). Note that this work (as well as all previous NEI calculations) ignores the possibility of removing more than a single electron from an atom at a time. Such processes as, for example, the Auger effect, occur frequently during photoionization by X-rays and should also be effective during electron-impact ionization. The inclusion of multielectron ionization processes would result in more rapid removal of the outer-shell electrons at high electron temperatures than we would predict using equation (1). Photoionization (which we also neglect) would have a similar effect on the outermost electrons. However, at the temperatures and densities of interest for modeling the X-ray emission from SNRs, the low stages of ionization are short-lived (see Figs. 1 and 2), and as a result these simplifying assumptions will not seriously compromise the accuracy of the final calculation.

We have assumed the applicability of the coronal limit approximation, in which the rates are independent of electron density; the dependence on temperature though, is shown explicitly. The rates have been taken directly from the work of Raymond and Smith (1977 and subsequent revisions). Altogether, for each atomic species Z , there are $Z + 1$ versions of equation (1), coupled to form a system of first-order ordinary differential equations. In all previous NEI model calculations, this system has been solved by one of several numerical rou-

tines (Runge-Kutta, predictor-corrector, etc.) which have certain disadvantages, such as the need to choose integration timescales. We have developed a simple, straightforward solution based on a matrix representation of the system of differential equations: namely,

$$\frac{d\mathbf{F}}{dt} = n_e \mathbf{A} \cdot \mathbf{F}, \quad (2)$$

where \mathbf{F} is the vector of dimension $Z + 1$ containing the ion fractions and \mathbf{A} is the tridiagonal square matrix containing the rates in the combinations shown in equation (1). By using the eigenvalues and eigenvectors of matrix \mathbf{A} , the solution can be determined quite simply from the diagonalized system

$$\frac{d\mathbf{F}'}{dt} = n_e \boldsymbol{\lambda} \cdot \mathbf{F}'. \quad (3)$$

Here $\boldsymbol{\lambda}$ is the diagonal matrix containing the eigenvalues and $\mathbf{F}' = \mathbf{V}^{-1} \cdot \mathbf{F}$, where \mathbf{V}^{-1} is the inverse of the square matrix formed from the eigenvectors. Hence, the calculation of the ionization structure has been reduced to simple exponentiation and matrix multiplication once the eigenquantities have been determined.

The matrix \mathbf{A} is tridiagonal, nonsymmetric, and singular. The singularity can be removed by the normalization condition for the ionization fractions, $\sum F_i = 1$, which also, however, eliminates the tridiagonal nature of the matrix. The method we have used to determine the eigenquantities is the so-called Left-Right transformation of Rutishauser (1958), an iterative procedure which has yielded good convergence for the temperatures and atomic species considered in this project. Some of the algorithms from Rutishauser, such as the Left-Right transformation itself and a convergence-accelerating algorithm known as "sweeping," have been implemented in FORTRAN by Carnahan, Luther, and Wilkes (1969). We have found this program to be adequate for our purposes; it determines both the eigenvalues and eigenvectors directly.

For a grid of temperatures separated by 0.1 in the logarithm within the range $4.0 \leq \log_{10} T_e \leq 8.0$, we have stored the matrix of eigenvectors, the inverse of this matrix, and the eigenvalues for each of the species C, N, O, Ne, Mg, Si, S, Ar, Ca, Fe, and Ni. This has increased our disk storage requirement over what it would have been assuming that a similar temperature grid of only the rates was required ($\sim 1 \times 10^6$ bytes compared to $\sim 5 \times 10^4$ bytes), but it has decreased significantly the amount of computer time needed for producing each model. More importantly, we do not need to choose time scales for integrating the rate equations, which in general will be different from the dynamical time scale; we only need to consider the time scale for temperature change, which is easily derivable from the hydrodynamical development of the model. Using this method, it is possible to follow the NEI evolution of a model SNR to virtually any age, since, at later stages of evolution, although dynamical time scales increase, the temperature change (per unit time interval) decreases.

This eigenvalue method for solving the rate equations also allows for an independent check on our solution before beginning the numerical calculation. We have tested the eigenvalues and eigenvectors by computing $(\mathbf{A} - \boldsymbol{\lambda}) \cdot \mathbf{V}$, which should yield a zero vector. For most cases considered, we find that the length of this zero vector is $\sim 10^{-6}$ the smallest eigenvalue, which is within the accuracy of the calculation (about 6 decimal digits). There is some instability for the highest tem-

peratures in the Fe grid ($T > 10^{7.8}$ K) owing to dynamic range limitations of the machine, which evidences itself in the inability of the matrix calculation to follow the extremely rapid changes in the lowest ionization states of iron during the earliest times. However, the states in question (below Fe xvii) are short-lived at these temperatures and, in any case, do not contribute to the X-ray emission. Since the later time evolution of the higher ionization states of Fe is consistent with extrapolations of the lower temperature results, we are confident that this effect will not influence the accuracy of the final calculation.

We have also carried out a graphical check of the eigenquantities by plotting the ionization fraction versus the time parameter, $n_e t$. In Figures 1 and 2 we present plots of the relative ionization fractions for oxygen and iron assuming a constant electron temperature of $10^{6.5}$ K and an initially completely un-ionized population. As a further check on the stability of our solutions, we have calculated these in two ways: first, using the un-ionized fractions as initial conditions for each time step; and second, using the fractions from the previous time step as the initial conditions for the next step. The two methods produce indistinguishable results. Further details concerning this matrix approach are found in the Appendix.

b) Numerical Hydrodynamic Shock Code

The dynamical evolution for our SNR models was calculated using a spherically symmetric hydrodynamic shock code based on the artificial viscosity method of Richtmyer and Morton (1967). We have used this code extensively in previous applications (e.g., Hughes, Helfand, and Kahn 1984) and have found that it agrees well with standard SNR evolution calculations. For this application we have included radiative cooling, but this has a negligible effect on the dynamics of such a young remnant. The electron temperature behind the shock is allowed to approach the ion temperature through the mechanism of Coulomb collisions; the lack of strong X-ray emission for Kepler's SNR above approximately 3.5 keV (see

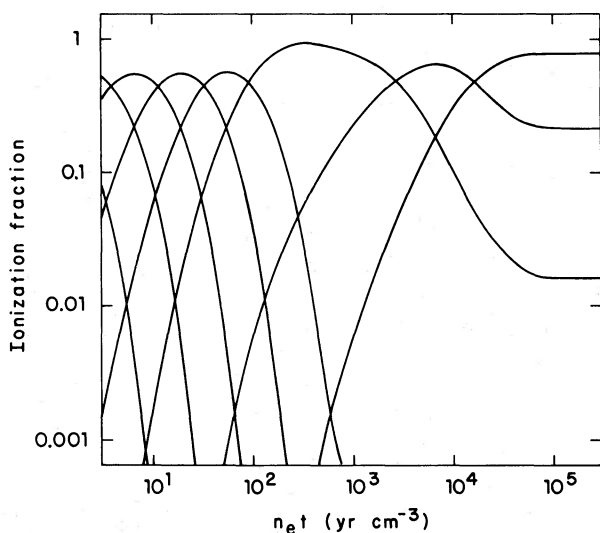


FIG. 1.—Plots of the relative ionization fraction versus the time parameter, $n_e t$, for the ion states of oxygen at a temperature of $10^{6.5}$ K. These were calculated using the matrix method discussed in the text. The states appear sequentially in time starting with O ii and ending with O ix. The prominent state at $n_e t \approx 10^{2.5}$ yr cm^{-3} is the helium-like ion O vii.

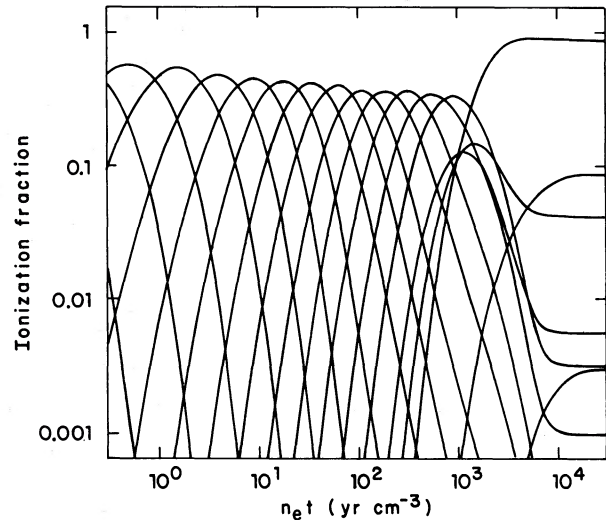


FIG. 2.—The same as Fig. 1 but for iron. Here the first state is Fe i and the last is Fe xix. The prominent state from $n_e t \approx 10^3$ yr cm^{-3} and beyond is the neon-like ion Fe xvii.

Becker *et al.* 1980a) favors this approach over that of setting the electron temperature equal to the ion temperature, a priori.

The model requires several input parameters: n_0 , the number density of the ambient circumstellar material; E , the energy of the supernova explosion; M_{ej} , the mass of ejecta; r_0 , the initial outer radius of the expanding shell of ejecta; and h , the ratio of the initial inner radius of the shell to r_0 . The astrophysically important parameters are n_0 , E , and M_{ej} , while r_0 and h determine the density (initially uniform) and range of velocity (increasing linearly with radius, as in a point explosion) in the ejecta. Ideally, one would like to set r_0 to the smallest possible value, but to avoid numerous rezonings of the radius grid, we have placed the initial radius of the ejecta at 0.05 pc for the models presented here. Other models run with $r_0 = 0.2$ pc were not significantly different from these with the single exception that, as expected, the final remnant radius was larger by 0.15 pc. For models in which the reverse-shock-heated ejecta produces most of the observed X-ray emission, the parameters n_0 , M_{ej} , and h , are most important since they determine the propagation speed of the reverse shock. Once an SNR has entered the Sedov phase, however, the ejecta becomes dynamically unimportant and the expansion depends only on E and n_0 .

We have produced emergent spectra from these remnant models using the X-ray emissivity of the various ionic and atomic species (extracted from our version of the Raymond and Smith 1977 code), which radiate in the *Einstein Observatory* bandpass. Total integrated spectra were obtained by adding together the emission from each ionic species in a given radial shell (determined from the electron temperature in that shell and weighted by its relative ionization fraction) and then summing over the radial shells comprising the volume of the remnant. The X-ray emission was calculated using both equilibrium and nonequilibrium ionization fractions. Furthermore, the emission from each atomic species was stored separately in order to allow us to vary the elemental abundances readily. Spatially resolved spectra, used in constructing model surface-brightness profiles, were determined by first calculating the line-of-sight distances through the set of radial shells which contribute at a given point in the two-dimensional projection

of the remnant on the sky. We then summed over those shells, combining the line-of-sight distances with the ionic X-ray emission (determined as above from the electron temperature in each shell weighted by the corresponding ionization fraction). The different atomic species (both for the equilibrium and non-equilibrium cases) were again stored separately.

III. CONSTRAINTS ON MODEL PARAMETERS FOR KEPLER'S SNR

The remnant of Kepler's SN (SN 1604) is the youngest of the historical galactic remnants with a well-determined age. Only recently has it been extensively observed in wavelength bands other than the optical; in the X-ray regime, the remnant has been studied only by the *Einstein Observatory*. Details of these X-ray observations can be found in Becker *et al.* (1980a) for the moderate-resolution spectra obtained with the solid state spectrometer (SSS), and in White and Long (1983) for the imaging and crude spectral observations obtained with the imaging proportional counter (IPC) and the high resolution imager (HRI). In the following section we describe our reanalysis of these data in light of the final reprocessing of the *Einstein* data base and our detailed models for SNR evolution. Here, we consider the constraints which can be placed on the range of model parameters as a result of some of the more direct observations of Kepler's SNR: an age of 376 yr determined from identifying the remnant with the explosion of 1604 (Baade 1943), an angular radius of $\sim 80''$ determined from both radio (Gull 1975a) and X-ray observations (see below and White and Long 1983), and the presence of only one bright ridge of emission in both the radio and X-ray images. This last observation implies that the remnant is either in the far Sedov regime or in the early stages of the reverse shock phase; models which have comparable emission from both the shocked ISM and the reverse shocked ejecta are not acceptable. This condition eliminates a wide class of models and imposes stringent limits on the amount of ejected mass contributing to the X-ray emission.

The constraints of age, size, X-ray brightness, and temperature (determined from fits of the IPC data to standard, equilibrium Raymond and Smith thermal plasmas) are applied differently to models in the Sedov phase, where we have an accurate similarity solution (Sedov 1959) and where the effects of nonequilibrium ionization are most dramatic, than to models in the reverse shock phase. We present both cases below.

a) Sedov Phase

For remnants which have swept up considerably more mass than they have ejected ($M_{sw} \gtrsim 10M_{ej}$), the SNR dynamical evolution is described by the Sedov relation between radius and age, where

$$r = 13(E/10^{51} \text{ ergs})^{1/5} n_0^{-1/5} (t/10^4 \text{ yr})^{2/5} \text{ pc} . \quad (4)$$

In the case of Kepler's SNR, the age at the time of observation was 376 yr and the angular size $\theta \approx 80''$, so that we can rewrite

equation (4) as a constraint for E , n_0 , and D , the distance to the remnant, as

$$\frac{E/10^{51} \text{ ergs}}{n_0} = 0.052(\theta/80'')^5 (D/5 \text{ kpc})^5 . \quad (5)$$

In Table 1 we present some values for n_0 (col. [1]) and E (col. [2]) using $\theta = 80''$ and a distance of 5 kpc. In column (3) we give the parameter $n_0^2 E$, which, along with the shock temperature, characterizes the X-ray spectrum from NEI plasmas (see Hamilton, Sarazin, and Chevalier 1983 for a complete discussion of this point). The temperature immediately behind the shock calculated using the Sedov relations and those from the hydrodynamics code are shown in columns (4) and (5). In SNR models where electron-ion temperature equilibration is not imposed, the electron temperature approaches a constant value near the center of the model remnant. A handy analytic approximation for this central plateau temperature has been derived by Cox and Anderson (1982). They find that

$$T_e \approx 1.4 \times 10^7 \text{ K} (T_s/10^6 \text{ K})^{1/15} E_{51}^{2/15} n_0^{4/15} . \quad (6)$$

Using the shock temperature from the Sedov solution in the above equation, we obtain the values quoted in column (6) of Table 1. These compare well with the results from the numerical code given in column (7).

As with most galactic SNRs, the distance to Kepler is not well known; estimates in the literature range from ~ 3.2 kpc (Danziger and Goss 1979) up to ~ 9 kpc (van den Bergh and Kamper 1977). However, our results at one distance can be used to constrain the parameters required at another distance in the following way. Suppose that we have determined a model which has (approximately) the correct surface brightness profile at some distance D . Then we can write

$$S = n_0^2 d \Lambda(T_s, n_0^2 E) , \quad (7)$$

where Λ represents the NEI emission, d is a characteristic line-of-sight path-length distance through the remnant, and S is the surface brightness. As we vary the distance to the model, d varies in direct proportion. If we assume that Λ is slowly varying with T_s and $n_0^2 E$, then to produce the same value of S at a different distance, n_0 must vary as $D^{-1/2}$. In Table 2 we present the model parameters corresponding to various distances, where we have used our model at a distance of 5 kpc with a density of 6 cm^{-3} as the case which agrees with the data (see § IV). The electron temperature, as determined by equation (6), varies by less than a factor of 2, justifying our assumption that Λ depends only weakly on T_s . The explosion energy ranges over two orders of magnitude for the given range of distances. Since, as we shall see, the assumption of Sedov conditions requires a very low ejected mass for Kepler (and thus a Type I explosion), distances much smaller or larger than these are excluded based on the observed energies of Type I SNs. Notice

TABLE 1

MODEL PARAMETERS FOR 5 kpc DISTANCE

n_0 (cm^{-3}) (1)	E (ergs) (2)	$\log_{10}(n_0^2 E)$ (3)	$\log_{10} T_s$ (Sedov) (4)	$\log_{10} T_e$ (model) (5)	$\log_{10} T_e$ (Cox and Anderson) (6)	$\log_{10} T_e$ (model) (7)
3.0	1.5×10^{50}	51.1	7.72	7.77	7.28	7.23
6.0	3.0×10^{50}	52.0	7.72	7.64	7.40	7.34
10.0	5.0×10^{50}	52.7	7.72	7.74	7.49	7.45

TABLE 2
MODEL PARAMETERS FOR VARIOUS DISTANCES

D (kpc) (1)	n_0 (cm^{-3}) (2)	E (ergs) (3)	$\log_{10}(n_0^2 E)$ (4)	$\log_{10} T_s$ (Sedov) (5)	$\log_{10} T_e$ (Cox and Anderson) (6)
3.0	7.7	3.1×10^{49}	51.3	7.28	7.27
4.0	6.7	1.2×10^{50}	51.7	7.52	7.33
5.0 ^a	6.0	3.0×10^{50}	52.0	7.72	7.40
6.0	5.5	7.1×10^{50}	52.3	7.88	7.45
7.0	5.1	1.4×10^{51}	52.6	8.01	7.49
8.0	4.7	2.6×10^{51}	52.8	8.13	7.52

^a Model compares favorably with data.

too how the density is constrained to a value $6 \pm 2 \text{ cm}^{-3}$, confirming the result of White and Long (1983).

b) Reverse Shock Phase

When a remnant has not swept up a large amount of interstellar material, the ejecta are important, both for the dynamical evolution and the X-ray emission. This phase is sometimes referred to as the free expansion phase, in which the ejecta expand with constant speed, but in fact, the ejecta must be decelerated in order for a reverse shock to appear and produce X-ray emission. In order to visualize the dependence of radius, X-ray luminosity, and shock temperature on the available model parameters, we have run a grid of shock models in which we require the surface brightness in the shocked ISM to be at least an order of magnitude dimmer than that in the ejecta (thus meeting the constraint of a single bright ring of emission). We have specified each model with three parameters: M_{ej} , the ejected mass; E , the energy of the explosion; and n_0 , the number density of the ambient medium. We have set the uniform density shell of ejecta to extend initially from 0.04 pc to 0.2 pc. The outer radius was chosen to be this large in order to avoid numerous rezonings of the radius grid during each calculation; as discussed in § II, it has virtually no effect on the luminosity. Varying the radius of the inner edge of the ejecta has only a slight effect on the emergent luminosity until the inner edge of the ejecta begins to approach the outer radius, i.e., when the shell becomes very thin (inner radius of ~ 0.19 pc). In this case, the reverse shock passes through the entire shell of ejecta at very early stages of the evolution, before significant adiabatic decompression has occurred. Thus, the temperature of the reverse shock is moderately low ($\lesssim 10^{6.8}$ K) and the density is high; cooling in the shell proceeds rapidly as a result of further expansion and radiative losses. The net effect is a greatly decreased X-ray luminosity because of the low ejecta temperature. Such a thin shell of ejecta is, however, inconsistent with a point explosion, as well as with the large range of speeds observed in supernova ejecta (Branch 1981).

In order to demonstrate the deceleration of the ejecta for the grid of models run, we have plotted the ejected mass versus the radius of each model at an age of 376 yr in Figure 3. Results for four different ISM densities, 0.3, 0.6, 1.2, and 1.8 cm^{-3} , are plotted. Furthermore, since a single explosion energy of 10^{51} ergs was used in all these models, there is a one-to-one correspondence between ejected mass and the maximum initial speed in the ejecta, which labels the top axis. The distance labeled on the right side corresponds to the observed angular size of $80''$. As expected, the models with the higher values of ISM density show the most deceleration and, as the ejecta

velocity in the model decreases, the final radius approaches the free expansion radius more closely.

In Figure 4, we plot ejected mass versus the HRI count rate from the northern half of the remnant² for the same set of models. The observed HRI rate is the dotted line at 0.9 s^{-1} . The model count rates were determined using solar elemental abundances and an absorbing hydrogen column density of $N_H = 10^{21.5} \text{ cm}^{-2}$, with distances chosen such that the peak of the radial surface brightness of each model was at $80''$. The rise

² Toward the north, the appearance of Kepler's remnant is consistent with the limb-brightening characteristic of a symmetric shell (see Figs. 10 and 15). This is not true for the remnant as a whole—the southern limb of the remnant is quite faint and shows little evidence of limb brightening. Since our SNR models are spherically symmetric, we have chosen to compare the count-rate data from the northern section of the remnant, where the shock appears most prominently, with the total model count rates divided by two. In this way our models are guaranteed to match the average surface brightness data from the north.

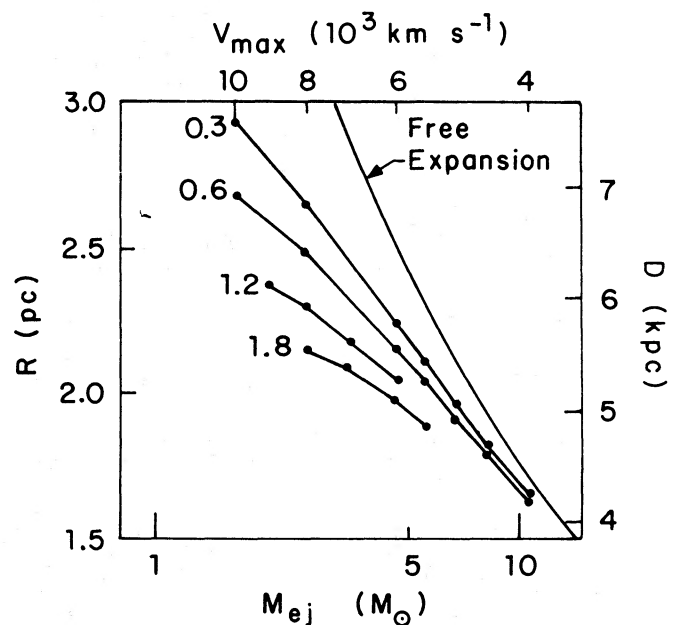


FIG. 3.—Plots of the ejecta radius at 376 yr versus supernova ejected mass, using an initial explosion energy of 10^{51} ergs, for models in the reverse-shock phase. The curves are labeled with the values of ambient circumstellar hydrogen number density used. The line representing the radius expected for undecelerated or free-expansion motion is also presented. The top axis is labeled by the maximum initial value of velocity in the ejecta, and the right axis is labeled by the distance assuming an $80''$ size. Note that the vertical axis is linear.

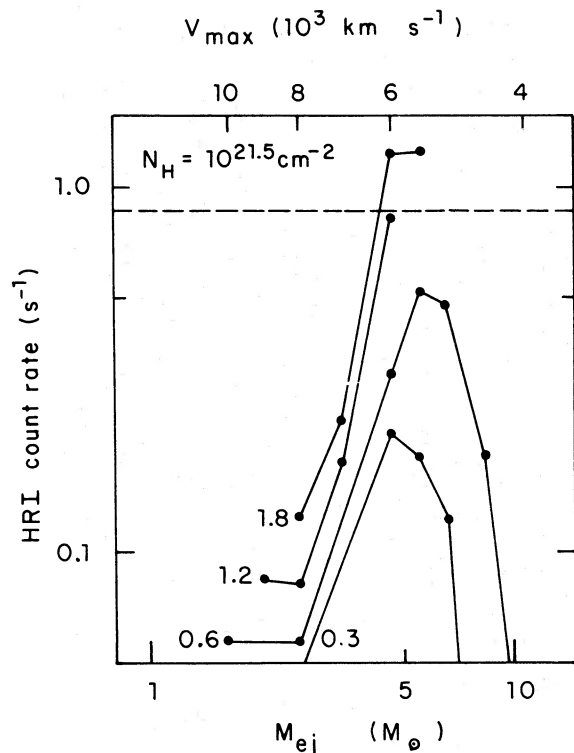


FIG. 4.—Plots of the expected model HRI count rate at 376 yr versus supernova ejected mass for the same set of models as in Fig. 3. The observed HRI count rate from the northern section of Kepler's SNR is the dotted line near the top. The column density to the source was taken to be $10^{21.5}$ H atoms cm^{-2} , and solar elemental abundances were used in all cases. The spherically symmetric total model count rates were divided by 2 for comparison with the data.

in count rate as the ejected mass increases from about 3 to $4 M_{\odot}$ is a result of the higher densities in those models. The decrease in count rate at even greater ejected masses ($> 7 M_{\odot}$) arises from the lower temperature of the ejecta in these cases. The electron temperature is so low that the emitted spectra fall below the HRI energy bandpass. This is shown clearly in Figure 5, where we have plotted ejected mass versus the maximum electron temperature in the ejecta, again for the same models. The falloff in temperature with increasing mass is quite evident. The stippled region corresponds to the range of temperatures derived from the spectral analysis of the IPC data compared to standard Raymond and Smith (1977) equilibrium ionization thermal plasmas. We have found that the temperatures in the reverse shock must be within (or near) this range in order to fit the observed spectra, even when nonequilibrium effects are included (see § IV). This is a result of the relatively high ejecta densities which speed the approach of the ionization fractions toward equilibrium: since the reverse shock propagates inward, the densest portion of the ejecta has been shocked for the longest time and thus will be closest to equilibrium.

It is clear that we can obtain a tight range on the model parameters from the preceding analysis. We have combined Figures 4 and 5 by plotting the maximum electron temperature in the ejecta versus the HRI count rate from the north, for each of the models (Fig. 6). On this figure the data for Kepler are presented as the cross-hatched line near the upper right. Clearly the only way to simultaneously satisfy the observa-

tional requirements of count rate and temperature is with a model having $\sim 4 M_{\odot}$ of ejecta expanding into an ISM density of $\sim 1.8 \text{ cm}^{-3}$. This conclusion is insensitive to the distance to the remnant and depends only weakly on the explosion energy: models with an explosion energy of 5×10^{50} ergs still require $\geq 3 M_{\odot}$ of ejecta and ISM densities greater than 1 cm^{-3} .

The amount of ejected mass is sensitive to the assumed elemental abundances. However, we find that for hydrogen- and helium-dominated plasmas (as above), the abundances derived from fits to the SSS spectrum do not significantly increase the total X-ray emission above that obtained with solar abundances (see the discussion of the reverse shock model in § IVc). This is because, while the abundances of the silicon-group elements must be increased, the iron abundance is decreased. Thus we estimate that our results concerning the amount of ejecta and the density of the ambient medium should not have to be revised downward by more than $\sim 30\%$ when enhanced abundances are included to fit the SSS spectrum. On the other hand, we must point out that these results are not relevant for plasmas composed entirely of heavy elements, such as might result from the explosion of an accreting carbon-oxygen white dwarf. In this case the X-ray emission depends on the stratification of the ejecta into zones of different elements, possible mixing between these zones, and the position of the reverse shock in the ejecta, as well as the relative abundances of each of the elements under consideration. A self-consistent model for this scenario would involve several more free parameters

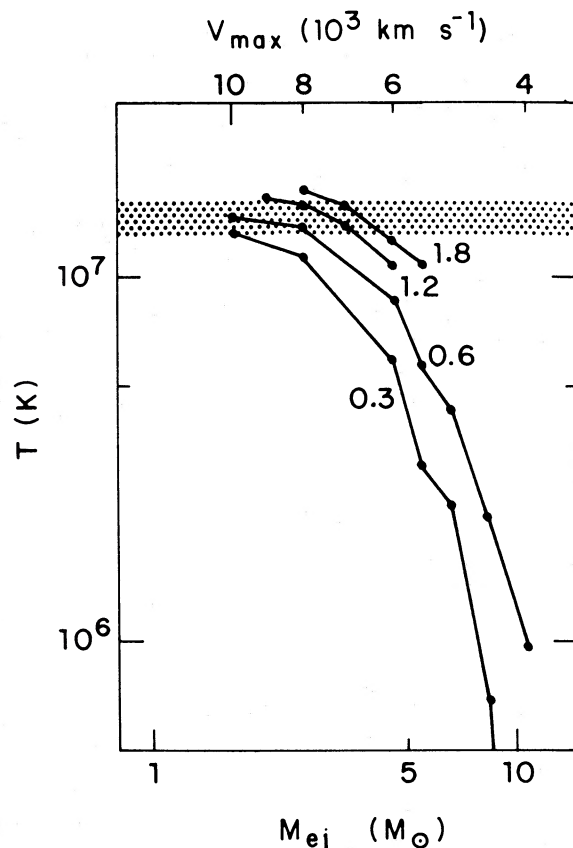


FIG. 5.—Plots of the maximum electron temperature in the ejecta at 376 yr vs. supernova ejected mass for the same set of models as in Fig. 3. The stippled region near the top corresponds to the temperatures determined from fitting the IPC data to standard equilibrium ionization Raymond and Smith thermal plasmas.

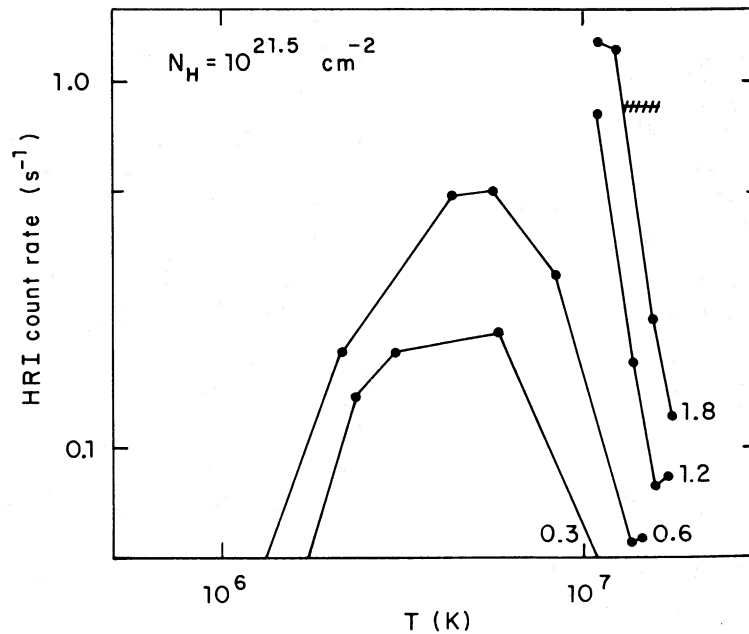


FIG. 6.—Plots of the expected HRI count rate from the northern half of the remnant vs. the maximum electron temperature in the ejecta for the models in Fig. 3 at 376 yr. This plot is a combination of Figs. 4 and 5. In this case, the crosshatched line in the upper right is the constraint obtained from the observed HRI count rate and temperature fit of the IPC data.

(abundances as well as zone sizes), and we have chosen not to pursue such models here.

In summary, we have derived constraints on the relevant parameters for two possible scenarios which may be applied to Kepler's SNR. For the Sedov case, we find $n_0 \approx 6 \text{ cm}^{-3}$ and $10^{50} \text{ ergs} \leq E \leq 10^{51} \text{ ergs}$ for a range of distances $4 \text{ kpc} \lesssim D \lesssim 7 \text{ kpc}$. These parameters are typical of a Type I SN explosion. In the reverse-shock case, we have $n_0 \approx 2 \text{ cm}^{-3}$, $M_{ej} \approx 4.5 M_\odot$, and $E \approx 10^{51} \text{ ergs}$, requiring a massive progenitor. Intermediate cases are excluded by the single peak in the remnant's surface-brightness profile. We now proceed to attempt a quantitative, self-consistent fit to all the extant X-ray data, highlighting the importance of NEI effects and exploring the heavy-element abundances required to explain the observed spectra.

IV. MODELS FOR KEPLER'S SNR: DETAILED COMPARISONS TO THE X-RAY DATA

a) The Data

Kepler's SNR was observed by the *Einstein* HRI twice during the lifetime of the spacecraft, once on 1979 September 29 and again on 1981 March 22, for 5600 s and 12000 s of effective exposure time respectively. During the interval between these observations, the efficiency of the instrument's photocathode is thought to have decreased as a result of cosmic-ray bombardment (Murray, 1984), and, in fact, we do observe a lower count rate from the source during the second pointing. We have combined the two observations by simply scaling up the count rate in the later pointing by $\sim 15\%$ to bring it into agreement with the earlier one.³ IPC data were obtained from a single pointing on 1979 September 20, and the data have undergone final reprocessing to eliminate uncer-

³ Our instrument effective area is based on calibration data taken before launch and does not include the loss of photocathode sensitivity; as such, it should be more representative of the earlier observation.

tainties in the gain-dependent energy response of the counter. In order to minimize the effects of energy-dependent spatial nonuniformities in the counter, we have determined an integrated IPC spectrum for the remnant by including counts within a circle of radius $3'$ and subtracting background from a blank, gain-matched field. Our effective area and spectral response matrix were obtained from the latest version of the IPC spectral analysis programs. Finally, the SSS data were also reprocessed and now extend to lower energies (Szymkowiak 1982) than does the spectrum published by Becker *et al.* (1980a); however, the data below $\sim 1 \text{ keV}$ are still uncertain owing to problems with icing on the detector window. We obtained the effective area and spectral response for the SSS from Becker (1981).

Below we discuss comparisons between these data and two particular models: one in which the shocked ISM generates most of the observed X-ray flux (the Sedov case), and one in which the X-ray emission comes predominantly from the reverse-shocked ejecta (the reverse-shock case). Both models were calculated to an age of 376 yr.

b) Sedov Models

In this case, the shocked ISM generates most of the observed X-ray flux, and the contribution from the ejecta is negligible. We have verified that an equilibrium ionization model with $E = 5.0 \times 10^{50} \text{ ergs}$, $n_0 = 10 \text{ cm}^{-3}$, and $M_{ej} = 0.5 M_\odot$, adequately fits the observed HRI surface brightness profile as determined by White and Long (1983). Since the X-ray emissivity from an NEI plasma is about an order of magnitude greater than that from the corresponding equilibrium ionization (EQI) plasma (for the densities and temperatures associated with this evolutionary phase), we have lowered the ISM density used in our models and found a good fit at 6 cm^{-3} with $E = 3.0 \times 10^{50} \text{ ergs}$ and $M_{ej} = 0.2 M_\odot$. At the age of Kepler, the mass of swept-up material is then $5.3 M_\odot$, considerably more than M_{ej} , and we find that the simi-

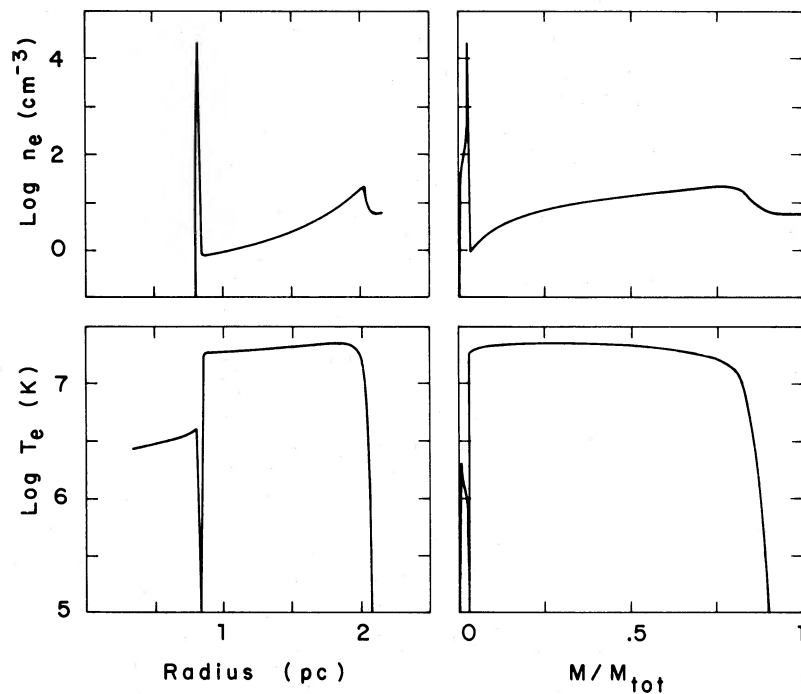


FIG. 7.—Plots of the electron temperature (*bottom panel*) and density (*top*) vs. radius (*left panel*) and fractional mass (*right*) in the interior of a model with $n_0 = 6 \text{ cm}^{-3}$, $E = 3 \times 10^{50}$ ergs, and $M_{ej} = 0.2 M_\odot$. This is referred to as the Sedov model.

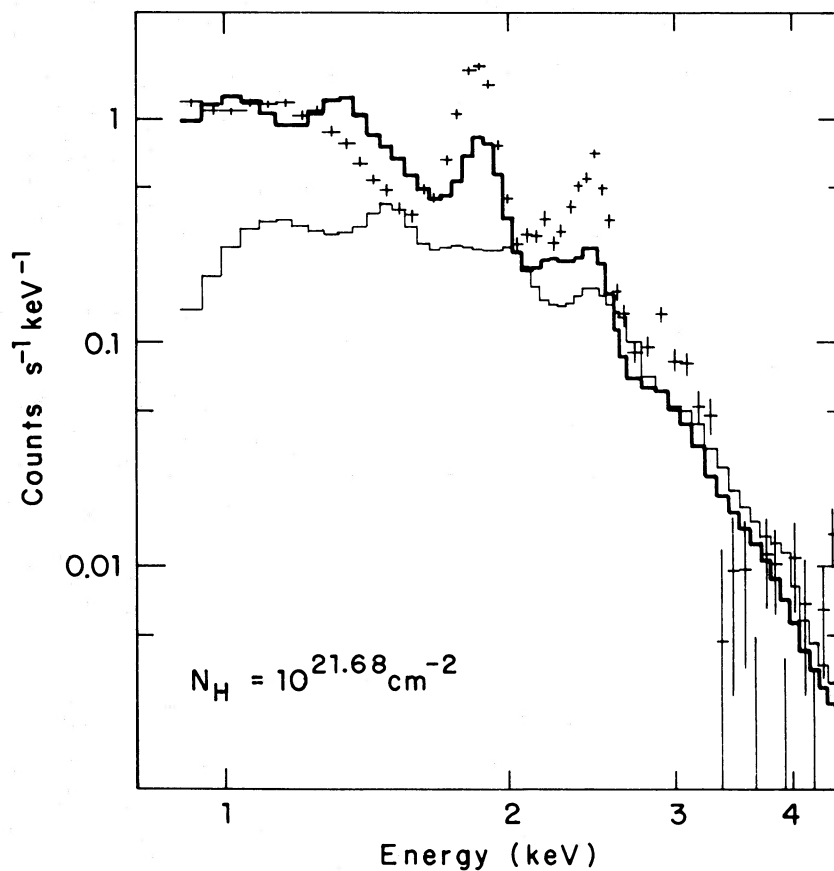


FIG. 8.—Comparison of the X-ray spectrum of Kepler's SNR as observed by the SSS and that expected from the Sedov model depicted in Fig. 7. The model spectra are for NEI (*bold line*) and for EQI (*thin line*), using solar elemental abundances. The column density was obtained from the best fit to the IPC spectrum using the NEI model.

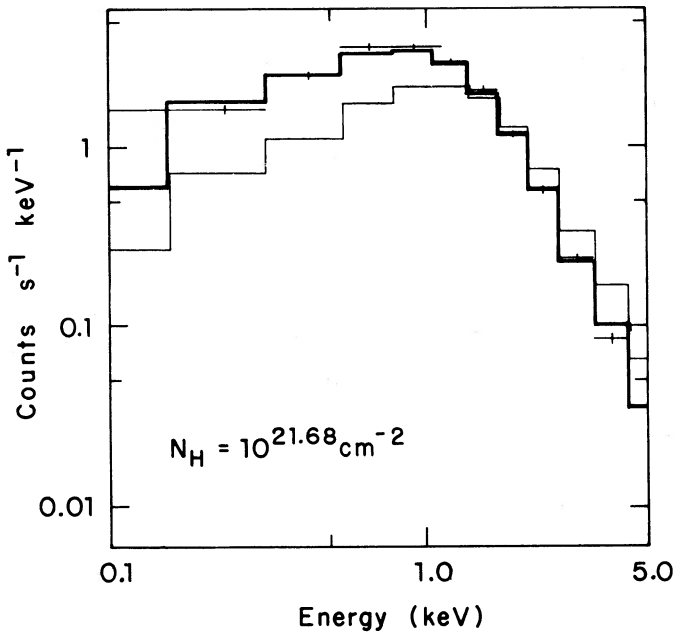


FIG. 9.—Comparison of the X-ray spectrum of Kepler's SNR as observed by the IPC with that expected from the Sedov model depicted in Fig. 7. The model spectra are for NEI (bold line) and for EQI (thin line), using solar elemental abundances.

larity solution of Sedov (1959) is a good approximation to the dynamics at this age. Plots of electron density and temperature are shown in Figure 7. The density varies from 21 cm^{-3} at the shock front to about 1 cm^{-3} near the center, and the temperature ranges from $10^{7.0} \text{ K}$ to $10^{7.3} \text{ K}$. The radius of the

shock front is 2.0 pc, and the bulk speed of the matter there is approximately 1500 km s^{-1} .

In Figures 8, 9, and 10 we present comparisons between this model and the X-ray observations made by the SSS, the IPC, and the HRI. The crosses represent the data, the bold line is the model spectrum or radial surface-brightness profile calculated using time-dependent ionization (NEI) fractions, and the thin line is the same quantity with EQI fractions. In each case we have convolved the model through an instrument-dependent effective area and then included the appropriate spectral (SSS and IPC) or spatial (HRI) broadening function. In these figures, we have assumed solar abundances for all atomic species throughout the whole remnant. The column density of absorbing material along the line of sight to the remnant is best determined from the IPC fit ($N_{\text{H}} = 10^{21.68 \pm 0.03} \text{ cm}^{-2}$), and we have adopted this value in presenting the other comparisons.

The introduction of NEI into the spectrum calculation is quite important for this case, since here the densest material is also the most recently shocked. The spectral character of the emission, both continuum and line emission, is totally different in the two cases. Furthermore the EQI model is at least a factor of 5 dimmer than the NEI model in the HRI bandpass, as can be seen in the comparison between the surface brightness profiles (Fig. 10). In an effort to improve the predicted spectra (particularly, the line intensities), we have varied the elemental abundances at different hydrogen-column densities and obtained the minimum χ^2 for $N_{\text{H}} = 10^{21.5} \text{ cm}^{-2}$ using the NEI model. In column (3) of Table 3 we present the abundances of Mg, Si, S, Ar, Ca, and Fe, relative to the solar values of Meyer (1979), which correspond to this minimum. The values which Becker *et al.* (1980a) found using a two-temperature equilibrium plasma are shown in column (4). Note that the abundances for our Sedov model are within a factor of 3 of standard

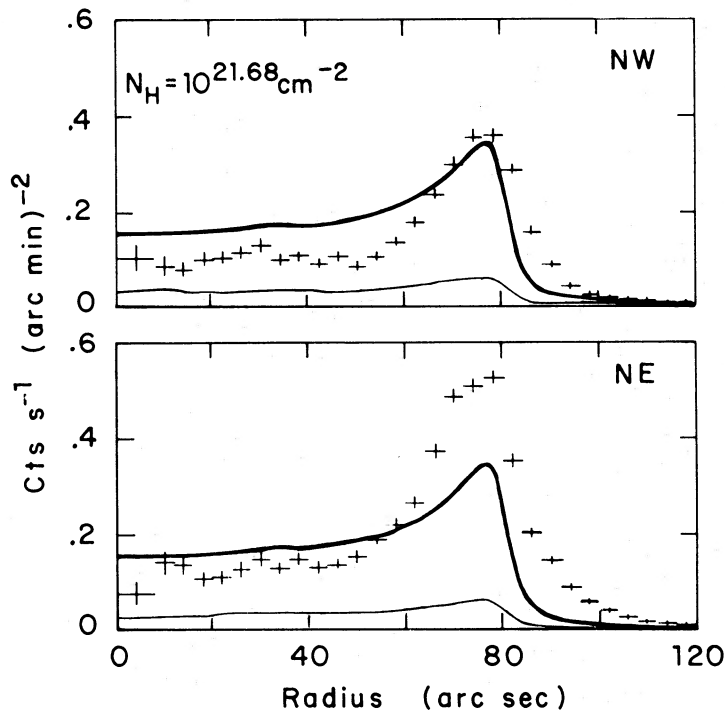


FIG. 10.—Comparison of the X-ray surface-brightness profile observed by the HRI and that expected from the Sedov model depicted in Fig. 7. The bold line is for the NEI case and the thin line for EQI. Both models use the best-fit column density from the IPC fit to the NEI model as well as solar elemental abundances.

TABLE 3
ELEMENTAL ABUNDANCES (RELATIVE TO SOLAR)^a FOR NONEQUILIBRIUM
IONIZATION SNR MODELS

Element (1)	Reverse Shock Case (2)	Sedov Case (3)	Equilibrium (Two-temperature) ^b (4)
Mg	0.003	0.3	0.20
Si	1.8	1.8	3.7
S	3.0	3.0	8.1
Ar	6.8	solar	19.1
Ca	2.4	solar	7.1
Fe	0.5	0.4	3.0

^a Meyer 1979.

^b Becker *et al.* 1980a.

solar abundances for all elements. As expected, the fit to the SSS data is much improved with these abundances (see Fig. 11), but surprisingly, the fit to the IPC data becomes worse. We believe that this is the result of the different energy bandwidths of the two spectral instruments: the IPC extends to lower (~ 0.2 keV) and higher (~ 4.5 keV) energies. At the low-energy end, the column density and line emission from carbon, nitrogen, and oxygen are most important, but this is where the SSS response is least well known because of the icing problems. At the high-energy end it is the inability of the SSS to constrain the continuum emission relative to the line emission, as discussed by Pravdo and Nugent (1983), which throws off the IPC

fit. Future observations of the high-energy continuum as well as a better determination of the hydrogen-column density should help to resolve this discrepancy.

The HRI surface-brightness profile has been determined from the data by examining counts from pie-shaped sectors of 90° in various sections of the remnant. As presented in White and Long (1983), the surface-brightness profile in the southern section of the remnant shows no evidence of limb brightening; we offer no explanation for this at the present time. In Figure 10 we compare the NEI and EQI model surface-brightness distributions with the data from two northern sections, the Northeast (NE) and the Northwest (NW). In both regions the center-to-edge variation is larger in the data than what is obtained from the model. It can be argued that this is the result of a local density enhancement at the north, which is not spherically-symmetric and which is just now being shocked by the passage of the blast wave. Such an enhancement (~ 1.5) would increase the X-ray luminosity from the remnant only at the edge and not through the center. However, aside from being ad hoc, this argument requires large circumstellar densities ($\sim 10 \text{ cm}^{-3}$) far (2 pc) from the progenitor star. As we will show below, a more natural explanation for the center-to-edge variation is afforded by the reverse-shock model.

From fitting the radial size of the HRI surface-brightness profile to the model, we derive a distance of 5.1 kpc. We can match the normalizations from the SSS and IPC spectra if we use this distance and include a factor of ~ 0.3 to account for the variation in brightness across the remnant. Since about

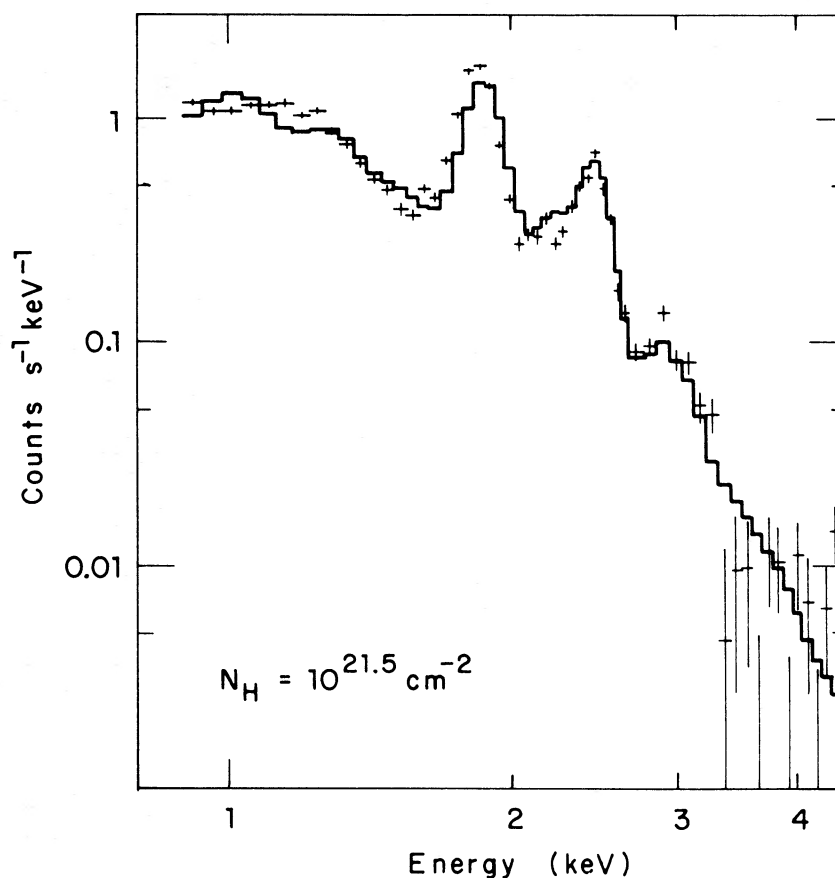


FIG. 11.—The expected SSS spectrum from the Sedov model calculated using the enhanced abundances given in Table 3. Only the NEI case is displayed.

one-third of the remnant exhibits a clear shock (the other two-thirds contributes less than about 30% to the total X-ray flux), this factor appears reasonable.

The ejected mass in this model was chosen to be as small as possible while still yielding a maximum bulk speed of about $12,000 \text{ km s}^{-1}$. (Recall that the explosion energy is set by the dynamical evolution.) This was accomplished by initially having all the ejecta in a thin shell which, as discussed in § III, keeps the temperature fairly low ($\lesssim 10^{6.2} \text{ K}$), in turn keeping the contribution of this material to the HRI surface-brightness profile sufficiently small. In principle, the allowable ejected mass could be raised in one of two ways: either by increasing the thickness of the ejecta shell while keeping the maximum speed the same, or by decreasing the maximum bulk-matter speed in the ejecta. If we try to remain consistent with the observed properties of Type I SNs, then the latter possibility is not viable, since decreasing the ejection speed significantly below about $12,000 \text{ km s}^{-1}$ is inconsistent with observations of extragalactic supernovae (Branch 1981). Increasing the thickness of the shell, however, will drive up the HRI emission, by increasing the temperature of the reverse shock. Enriching the ejecta in heavy metals will also increase the HRI emission. The surface-brightness profile certainly does not allow for any more emission in the interior of the remnant—it is too bright as it is.

It is possible (and perhaps likely), however, that the shell of ejecta has fragmented by now (since the reverse shock has passed through the entire shell) and that some mass is hidden in cool, dense clouds. We require that such clumps be denser than $\sim 10^3 \text{ cm}^{-3}$ (for cosmic elemental abundances) in order that they cool below $10^{5.5} \text{ K}$ in less than 350 yr. Clumps of ejecta enriched in elements with $Z \geq 3$ would cool more rapidly than this, and the density limit for metal-rich clouds would be correspondingly lower. It is also possible that some of the ejecta is now in the form of grains. Consequently, we

must view the value of $0.2 M_{\odot}$ as an upper limit to the mass of X-ray bright ejecta for this model.

c) Reverse Shock Models

Guided by the results of § III, we chose a model with $E = 10^{51} \text{ ergs}$, $M_{ej} = 4.5 M_{\odot}$, and $n_0 = 1.8 \text{ cm}^{-3}$. Clearly this model is not unique, and variations on the initial conditions will play a role in the details of the results, but the general features (such as the thin shell of moderately high-density material) are representative. We present plots of the electron temperature and density in the interior of the model in Figure 12. In this case, the X-ray-emitting gas has been heated to temperatures of $10^{6.5}$ – $10^{7.1} \text{ K}$ by the passage of a reverse shock through the ejecta. This hot matter lies between the contact interface separating the ejecta from the ISM, at a radius of 1.89 pc, and the location of the reverse shock, at approximately 1.85 pc. Inside this radius is $\sim 1.9 M_{\odot}$ of undecelerated cold matter. At the contact discontinuity, the bulk velocity of the matter is approximately 4500 km s^{-1} . There is also $\sim 1.9 M_{\odot}$ of shocked ISM extending from the contact interface out to a radius of $\sim 2.2 \text{ pc}$, with a maximum density of 7.5 cm^{-3} and temperatures ranging from $10^{6.8} \text{ K}$ to $10^{7.5} \text{ K}$. Although the mass of this material is comparable to that of the shocked ejecta, the mean density is almost two orders of magnitude smaller, and the X-ray emissivity is smaller by nearly the same factor.

From the position of the reverse shock out toward the contact interface, the density increases by more than four orders of magnitude, while the pressure increases by only one order of magnitude; thus, the temperature rises from the reverse shock outward, reaches a maximum, and then falls to a low value at the contact interface. We have compared this numerical model to the recently derived similarity solution of Hamilton and Sarazin (1984) and have found that the pressure

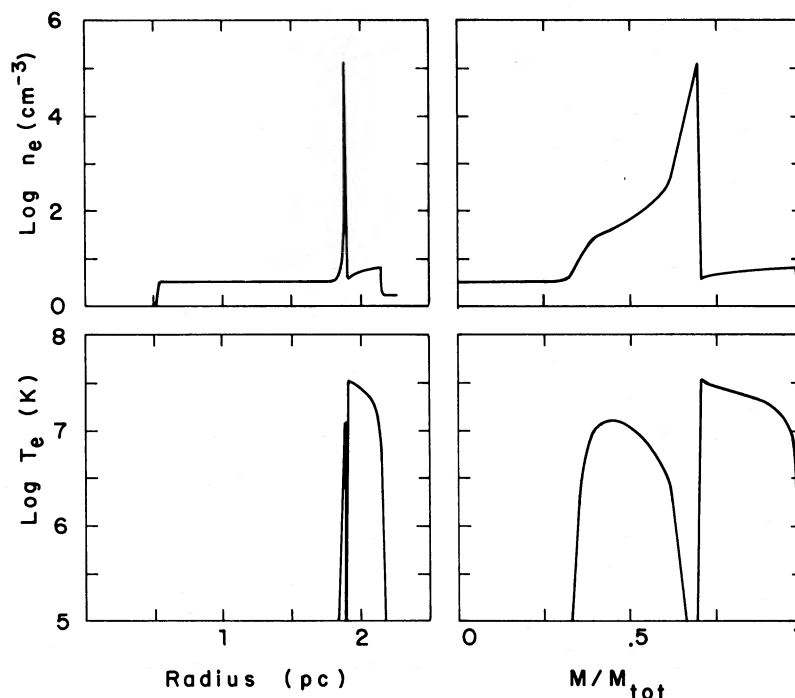


FIG. 12.—The same as Fig. 7 but for a model with $n_0 = 1.8 \text{ cm}^{-3}$, $E = 10^{51} \text{ ergs}$, and $M_{ej} = 4.5 M_{\odot}$, referred to as the reverse shock model

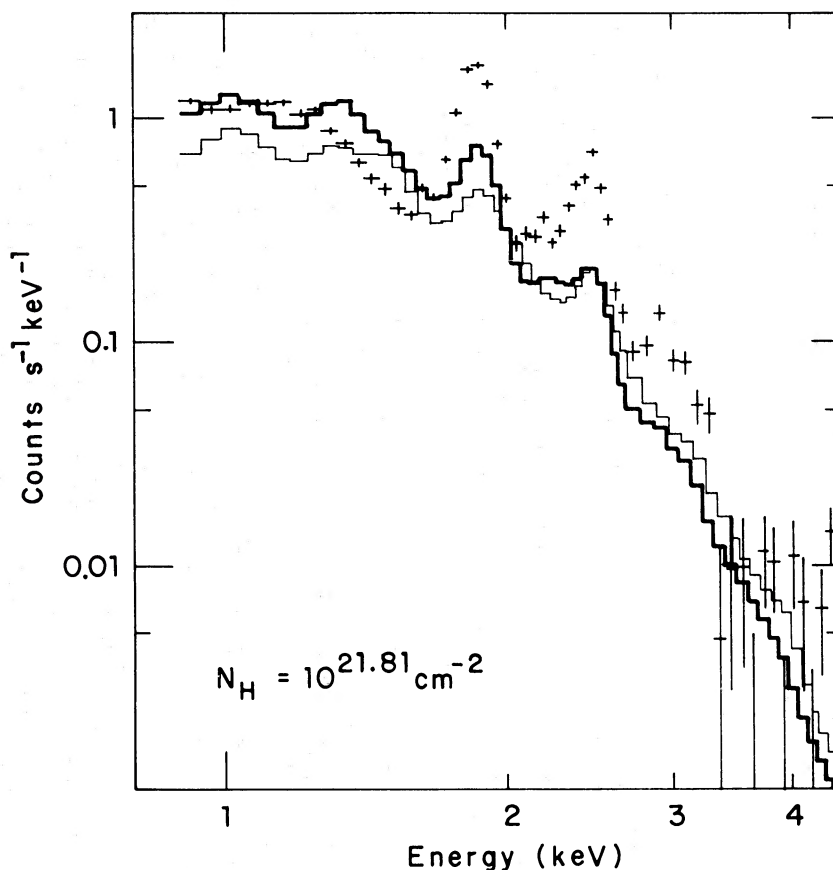


FIG. 13.—The same as Fig. 8 but for the reverse shock model

variation throughout the ejecta is greater than predicted by their analysis. Furthermore we find that the radius of the numerical model is larger (by a factor of ~ 2) than the maximum radius yielded by their equations. Both of these effects were also observed by Hamilton and Sarazin in their own comparisons to a numerical hydrodynamic calculation. These authors point out that the similarity solution may be a useful approximation to the internal temperature and density structure in the reverse shock but may not accurately reproduce the evolution of global quantities (such as the radius of the contact discontinuity). For comparison to the surface-brightness data, accurate positions for the reverse shock and the contact surface, such as are produced by our hydrodynamic code, are necessary.

The comparisons to the data are shown in Figures 13, 14, and 15, which are drawn in the same format as the Sedov-model figures of the preceding section, and again with solar elemental abundances. As before, we determined the absorbing hydrogen-column density ($N_{\text{H}} = 10^{21.81 \pm 0.03} \text{ cm}^{-2}$) from the IPC data and the NEI model. The NEI model clearly fits the IPC spectrum very well (Fig. 14), and although the EQI fit is somewhat poorer, an equilibrium spectrum could most likely also yield an acceptable fit with minor adjustments of the model parameters. The SSS data (Fig. 13), on the other hand, exhibit large deviations from the predicted spectra although a comparison between the two models is quite revealing, showing the lower ionization state which results from the NEI case. Note in particular the Si helium-like $1s2p-1s^2$ line at 1.9 keV, which is narrower and more intense than in the equi-

librium model. We also varied the abundances for this model; the χ^2 minimum for the SSS observation compared to the NEI model was obtained using a column density of $10^{21.8}$ H atoms cm^{-2} and the elemental abundances shown in column (2) of Table 3 (see also Fig. 16). As in the Sedov case, though, the fit to the IPC spectrum is worsened by this procedure for the same reasons as discussed above.

The HRI surface-brightness profile of this model is remarkably different from the Sedov case because of the different geometries of the X-ray emitting regions. The reverse-shock regime is geometrically very thin, so that the line-of-sight distance through it near the center is considerably smaller than at the edge, making for the large center-to-edge variation shown in Figure 15. The Sedov case has a much thicker emission region, and thus the center-to-edge variation in its surface brightness profile is correspondingly less (see Fig. 10). Furthermore, although the reverse-shock-model shock front seems to be thinner than the data, Rayleigh-Taylor instabilities at the contact interface will tend to fragment the outer edge of the ejecta (Gull 1973, Cowie 1975), broadening the peak of the surface brightness profile from the model. The distance of 4.9 kpc, required to match the profile, is in reasonable agreement with the normalization values obtained from the SSS and IPC spectral fits if a filling factor of approximately 0.3 is again included.

It is instructive to compare the Sedov and reverse-shock models. We see in Figures 8 and 13 how the NEI effects for a young remnant in the Sedov phase mimic the spectral character of a cooler, denser plasma closer to ionization equilibrium,

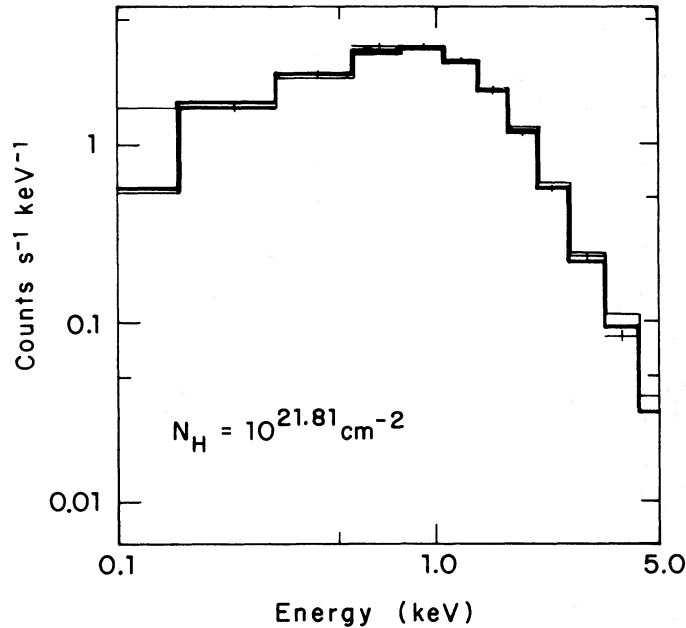


FIG. 14.—The same as Fig. 9 but for the reverse shock model

as exemplified by the reverse-shock case. This makes it difficult to discriminate between the models on the basis of broad-band spectra alone. However, the surface brightness profiles (Figs. 10 and 15) show considerable differences between the two cases even when NEI effects are included, and thus they serve as the best discriminators between models. Given the correct density inhomogeneity (as discussed above), the Sedov model could be made to fit the surface brightness as accurately as the reverse-shock model does, but the requirement that the emission from

the ejecta be negligible is an extremely powerful constraint working against this model. In the following section we discuss this in more detail.

V. DISCUSSION

By employing a novel approach to the problem of time-dependent ionization in a shock-heated plasma and coupling our solution to a spherically symmetric hydrodynamic calculation for the evolution of a point explosion in a uniform

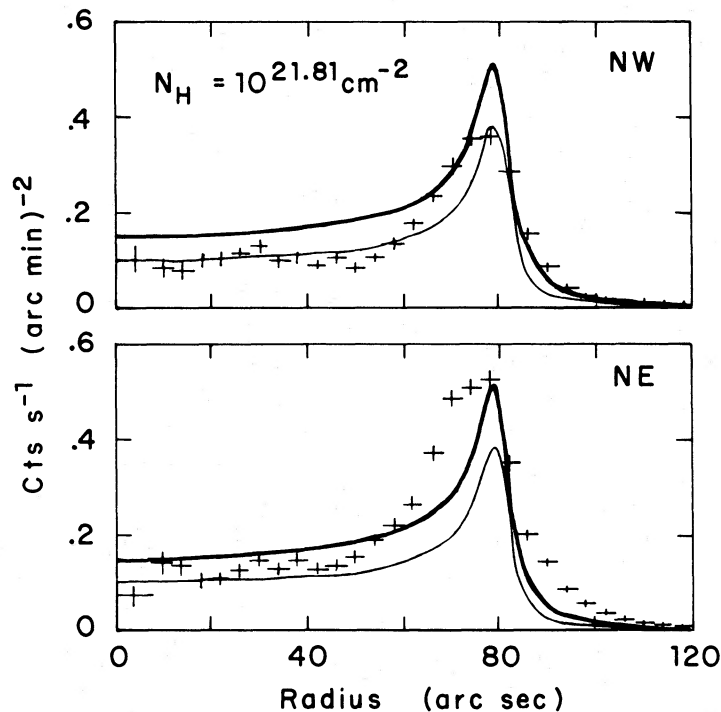


FIG. 15.—The same as Fig. 10 but for the reverse shock model

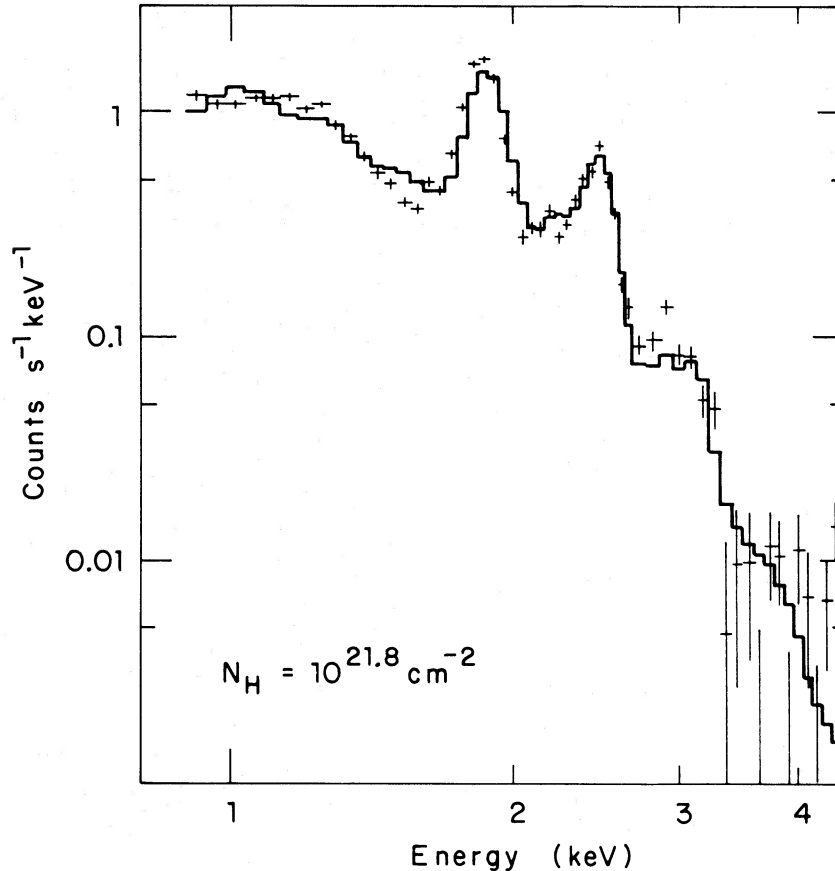


FIG. 16.—The same as Fig. 11 but for the reverse shock model

medium, we have produced a tool for exploring the evolution of X-ray emission from young SNRs. Applying this to Kepler's SNR, we find two narrowly constrained classes of models which can simultaneously fit the spectral and morphological features of the object: a Sedov model, in which the emission arises from shocked ambient gas; and a reverse-shock model, in which the SN ejecta is the dominant source of radiation. We have compared the emission from one specific model in each class with the radial surface brightness profile, the 0.2–4.5 keV broad-band spectrum, and the 1–3 keV moderate-resolution spectrum of the remnant, using data obtained with the *Einstein Observatory*. Reasonable fits were obtained in both cases, and we find that it is not possible to discriminate between these two scenarios using only the presently available X-ray observations.

High-dispersion X-ray spectra would allow us to examine directly the ionization state of the hot plasma and, perhaps, differentiate between temperature effects and ionization effects, so that a choice between the two models would become possible. Observations of the high-energy continuum, as well as limits on iron line emission above ~ 6 keV, would also serve as useful discriminators between models. For example, we have computed the flux expected in the iron-line complex from the two NEI models, using the atomic data from Mewe and Gronenschild (1981), and find that most of the flux will come from the $K\alpha$ lines of Fe XIX to Fe XXII at an energy of about 6.5 keV. For the reverse-shock case we expect 0.26×10^{-4} photons $\text{cm}^{-2} \text{s}^{-1}$ in the line, and for the Sedov case we expect

0.77×10^{-4} photons $\text{cm}^{-2} \text{s}^{-1}$, using solar iron abundance and a filling factor of 0.3.

While direct fits to the data do not allow us to distinguish which model actually describes Kepler's remnant, the constraints imposed suggest the perhaps surprising conclusion that the SN progenitor was a massive star. At a distance of 5 kpc, the remnant lies 600 pc above the galactic plane. Essentially all current models of the ISM predict a mean density at this height of less than $\sim 10^{-2} \text{cm}^{-3}$ (e.g., Cox and Smith 1974; McKee and Ostriker 1977), or a total mass of $\sim 10^{-2} M_{\odot}$ in the 10^{57}cm^3 volume swept out by the blast wave of the SN. Yet the surface brightness of the remnant requires that several solar masses of material are currently radiating at X-ray temperatures (assuming hydrogen- and helium-dominated plasmas; see below for metal-rich plasmas), and its current size demands an ambient medium with a density some two orders of magnitude higher than expected. These conclusions hold irrespective of the evolutionary state of the remnant and after explicitly taking into account the effects of time-dependent ionization on the emissivity of the gas. They are relatively insensitive to the remnant's distance and are unlikely to be altered by a large factor when such effects as electron conduction across the shock front, magnetic fields, and an inhomogeneous external medium are included in the calculation (see the Appendix of White and Long 1983 for details).

A sensitive interferometric map of the region in the 21 cm line could test whether or not the remnant is in fact expanding into a dense ($n \gtrsim 1 \text{cm}^{-3}$) interstellar cloud 600 pc above the

plane. If, however, we ignore this unlikely possibility, and assume that the ambient density resulted from mass loss prior to the SN, our model fits require a mass for the progenitor star of more than $\sim 7 M_{\odot}$. In the Sedov picture, the swept-up mass M_{sw} is $\sim 5 M_{\odot}$, and the visible ejected mass M_{ej} is less than $0.2 M_{\odot}$ with the possibility of additional unseen ejecta hidden in radiating cooled, dense clumps. Virtually all SN models require a core mass immediately prior to the explosion of more than $\sim 1.4 M_{\odot}$. Thus, if we assume that the shock has just reached the edge of the mass lost by the pre-SN star, we require a $\sim 6.5 M_{\odot}$ progenitor: $5 M_{\odot}$ of envelope material plus $0.2 M_{\odot}$ of hot ejecta plus $1.2 M_{\odot}$ more of core material in either cold gaseous clumps or an unseen collapsed object at the center of the remnant (no evidence for any compact remnant has been found, although a black hole or a quiescent neutron star could easily have escaped detection). If, on the other hand, the reverse-shock case applies, we have $M_{\text{ej}} \approx 4.5 M_{\odot}$ and $M_{\text{sw}} \approx 2 M_{\odot}$, again requiring a progenitor of more than $\sim 6.5 M_{\odot}$. The fate of the pre-SN core is uncertain in this case, although it could well have been disrupted completely.

We are unable to sustain this conclusion of a high-mass progenitor for a reverse-shock model composed entirely of heavy ($Z \geq 3$) elements. The very high specific luminosity of metal-rich plasmas requires us to lower the ejected mass to fit the surface brightness data and the total observed luminosity; a value of $\sim 1 M_{\odot}$, expected in current models of exploding carbon-oxygen white dwarfs, could produce sufficient X-ray emission. Given this mass, though, we can use Figure 3 to obtain an approximate value for the ambient density necessary to decelerate the ejecta. With a circumstellar density of $\sim 0.3 \text{ cm}^{-3}$, the remnant would have to be at a distance of $\sim 8 \text{ kpc}$ to fit the observed radius. A value of 0.1 cm^{-3} is probably a lower limit to the density in order that the derived distance remain less than $\sim 10 \text{ kpc}$. Such a value for n_0 is still much larger than the predicted value for the ISM at this z (now greater than $\sim 1 \text{ kpc}$ given these larger distances), implying that the progenitor star must still have modified its surroundings before exploding. The progenitor mass for this extreme case could be as low as $\sim 2 M_{\odot}$: pre-SN wind material extending just to the current position of the shock of $\sim 1 M_{\odot} \approx M_{\text{sw}}$ and $M_{\text{ej}} \approx 1 M_{\odot}$. The progenitor, then, must still be a Population I object (cf. Oemler and Tinsley 1979).

The probability of finding such a star more than 500 pc from the galactic plane is small but distinctly nonzero. Garmany, Conti, and Chiosi (1982) have found that $\sim 4\%$ of all O stars ($M > 20 M_{\odot}$) within 2.5 kpc of the Sun have $|z| > 200 \text{ pc}$; within 5 kpc , 50 such stars are known. For the much more numerous and longer-lived B stars, there are 10^4 objects with $D \leq 5 \text{ kpc}$ and $|z| \geq 500 \text{ pc}$ (Allen 1973); if we restrict ourselves to stars earlier than B5 ($M > 6.5 M_{\odot}$), we still expect $\sim 10^3$ stars within this distance from the Sun at $|z| \geq 500 \text{ pc}$. The lifetime for a B5 star is $\sim 6 \times 10^7 \text{ yr}$; a value of $v_z \approx 75 \text{ km s}^{-1}$ is sufficient for the star to reach 600 pc before it leaves the main sequence. Given these statistics, the probability of a star with $D \leq 5 \text{ kpc}$, $|z| \geq 500 \text{ pc}$, and $M \geq 6.5 M_{\odot}$ having exploded in the last 10^3 years is $\sim 5\%$. This scenario is further strengthened by noting that such an explosion in or near the galactic plane would have been undetectable unless it were extremely close, owing to the large optical extinction in the plane—the only Population I SNs we should expect to see are those occurring at high latitudes.

The historical records for Kepler's SN have been interpreted as being consistent with the light curve of a Type I event

(Baade 1943; Clark and Stephenson 1977). Recent efforts to model Type I SNs have concentrated on two general classes of models: accreting white dwarfs pushed over the Chandrasekhar limit, and single stars in the range $7 M_{\odot} \lesssim M \lesssim 10 M_{\odot}$ (see, e.g., Wheeler 1980 for reviews). Our results exclude the white dwarf case unless either (1) the system just happened to be passing through a dense interstellar cloud ($\sim 6 \text{ cm}^{-3}$) 600 pc out of the plane where it exploded; or (2) more than half the gas we see at X-ray temperatures is in heavy elements, the source is at a distance of $\sim 10 \text{ kpc}$, and at least $\sim 1 M_{\odot}$ of ambient material has recently been shed by the accreting dwarf's companion. Both possibilities are testable: the first via 21 cm observations of the remnant's vicinity, and the second through higher resolution X-ray spectral data and further modeling. To us, each seems somewhat contrived.

The possibility of intermediate-mass SN I progenitors is, however, not unattractive. Such stars consist of hydrogen envelopes comprising $\sim 80\%$ of their total mass surrounding $1.5\text{--}2.5 M_{\odot}$ degenerate cores. Before exploding, such a star becomes a red giant and presumably sheds a significant fraction of its envelope in a cool stellar wind. The red supergiant IRC +10216 may be an example of such a star. It has a mass-loss rate of $1.5 \times 10^{-4} M_{\odot} \text{ yr}^{-1}$ in a wind with an outflow velocity of 17 km s^{-1} , a rate which has continued for at least $14,000 \text{ yr}$ (Knapp *et al.* 1982). Furthermore, the envelopes around a number of similar stars indicate total main sequence masses greater than $\sim 6 M_{\odot}$ (Knapp *et al.* 1982). Since $\sim 2.1 M_{\odot}$ has been lost to date from IRC +10216, the star could explode anytime in the next $2 \times 10^4 \text{ yr}$ and produce $2\text{--}4 M_{\odot}$ of ejecta (the dissipated core plus any remaining envelope material) moving into a medium with a large n_0 (the wind material). These are similar to the parameters required by the reverse-shock fit to Kepler's remnant.

One direction of our future work will be to evolve such an explosion in an ambient medium where $n_0 \sim r^{-2}$ as would be expected from material lost in a stellar wind. Including ejecta composed of only heavy elements is also an important item. Observational programs will focus on defining the high-energy X-ray continuum and line emission from the source and on determining the characteristics of the ISM in the remnant's vicinity. Coupled with a similar self-consistent analysis of the other young Type I remnant, Tycho's SNR, our approach may lead to significant progress in identifying the progenitors of Type I events and in defining their contributions to the population of compact objects in, and nucleosynthetic evolution of, the Galaxy.

Note added in manuscript 1984 December 6.—After this work was completed, we obtained a revised HRI effective area, based on in-flight calibration data, which results in nearly a factor of 2 increase in the calculated count rates over that expected from our present version of the HRI response. The largest effect of this change on our work here would be to lower the derived circumstellar density in the Sedov case from 6 cm^{-3} to $\sim 4.5 \text{ cm}^{-3}$ (still within our quoted errors nevertheless); none of our conclusions (particularly those regarding a Population I progenitor) are significantly affected.

We wish to thank Gary Chanan and Steve Kahn for inspiration during the course of this work and for many helpful comments. Thanks are also extended to R. L. White, who developed the hydrodynamic code and who was always willing to discuss it. Finally, we offer our heartfelt gratitude to the

which Rutishauser's method is optimal. This is not true for the nonsingular matrix, which acquires nontridiagonal elements in the following way.

As an example we eliminate the first ionization state by using

$$F_1 = 1 - \sum_{i=2}^n F_i.$$

This changes the equation for the time evolution of the second ionization state to

$$\frac{dF_2}{dt} = -(\alpha_1 + \alpha_2 + R_1)F_2 + (R_2 - \alpha_1)F_3 - \alpha_1 \sum_{i=4}^n F_i + \alpha_1, \quad (\text{A2})$$

while the other equations for F_3 to F_n remain unchanged. This introduces a row of non-zero elements into the top row of the reduced (nonsingular) matrix, now of dimension $n - 1$. Note that the constant term in equation (A2) above can be eliminated by a shift in the origin of the ionization fractions

$$F'_i = F_i - F_i^{\text{EQI}}, \quad i = 2, \dots, n,$$

where F_i^{EQI} are the equilibrium ionization fractions. This result can be derived straightforwardly; note that it arises because of the removal of the zero eigenvalue, which has the equilibrium ionization fractions as its eigenvector.

The eigenvalues and eigenvectors of the reduced matrix can be determined using the Left-Right transformation and, although this matrix is not optimized for this method, the results obtained are superior to those from the singular matrix. This is in part due to the smaller matrix dimension, but primarily it arises from constructing the complete ($n \times n$) matrix of eigenvectors by including an additional row and column in the following manner. The equilibrium ionization fractions (calculated quite accurately by independent methods) are used as the additional column; and for the components of the additional row, the negative sum of that column's components is inserted. This ensures that the sum of the components in each column equals zero (to conserve ion population), except for the column containing the equilibrium fractions. The virtue of this method is that the solution is guaranteed to approach the equilibrium ionization fractions with considerable accuracy. Such a statement is not possible for the eigenvalues and eigenvectors calculated from the singular matrix. We have carried out several numerical tests on the Si rate matrix (15×15) which confirm these conclusions.

The final point we must address is the possibility of degenerate eigenvalues. In theory the algorithm used to determine eigenvectors would have to be modified in the case of multiple eigenvalues. An additional constraint, such as orthogonality between the eigenvectors of the degenerate eigenvalues, would have to be applied. In practice, however, it has not been necessary to resort to this procedure. No two eigenvalues of any single matrix in our grid have been closer than $\sim 0.5\%$, and even the worst case has not caused any numerical instability when the standard algorithm was utilized.

REFERENCES

- Allen, C. W. 1973, *Astrophysical Quantities* (London: The Athlone Press), p. 251.
- Baade, W. 1943, *Ap. J.*, **97**, 119.
- Becker, R. H., Boldt, E. A., Holt, S. S., Serlemitsos, P. J., and White, N. E. 1980a, *Ap. J. (Letters)*, **237**, L77.
- Becker, R. H., Holt, S. S., Smith, B. W., White, N. E., Boldt, E. A., Mushotzky, R. F., and Serlemitsos, P. J. 1979, *Ap. J. (Letters)*, **234**, L73.
- . 1980b, *Ap. J. (Letters)*, **235**, L5.
- Becker, R. H., Szymkowiak, A. E., Boldt, E. A., Holt, S. S., and Serlemitsos, P. J. 1980c, *Ap. J. (Letters)*, **240**, L33.
- Becker, R. H. 1981, private communication.
- Branch, D. 1981, in *Supernovae: A Survey of Current Research*, ed. M. J. Rees, and R. J. Stoneham (Dordrecht: Reidel), p. 267.
- Carnahan, B., Luther, H. A., and Wilkes, J. O. 1969, *Applied Numerical Methods* (New York: Wiley), p. 236ff.
- Clark, D. H., and Stephenson, F. R. 1977, *The Historical Supernovae* (New York: Pergamon), p. 191.
- Cowie, L. L. 1975, *M.N.R.A.S.*, **173**, 429.
- Cox, D. P., and Anderson, P. R. 1982, *Ap. J.*, **253**, 268.
- Cox, D. P., and Smith, B. W. 1974, *Ap. J. (Letters)*, **189**, L105.
- Danziger, I. J., and Gorenstein, P., eds. 1983, *IAU Symp. 101, Supernova Remnants and Their X-Ray Emission* (Dordrecht: Reidel).
- Danziger, I. J., and Goss, W. M. 1979, *M.N.R.A.S.*, **190**, 47.
- Garmany, C. D., Conti, P. S., and Chiosi, C. 1982, *Ap. J.*, **263**, 777.
- Giacconi, R., et al. 1979, *Ap. J.*, **230**, 540.
- Gronenschild, E. H. B. M., and Mewe, R. 1982, *Astr. Ap. Suppl.*, **48**, 305.
- Gull, S. F. 1973, *M.N.R.A.S.*, **161**, 47.
- . 1975a, *M.N.R.A.S.*, **171**, 237.
- . 1975b, *M.N.R.A.S.*, **171**, 263.
- Hamilton, A. J. S., Sarazin, C. L., and Chevalier, R. A. 1983, *Ap. J. Suppl.*, **51**, 115.
- Hamilton, A. J. S. and Sarazin, C. L. 1984, *Ap. J.*, **281**, 682.
- Hughes, J. P., Helfand, D. J., and Kahn, S. M. 1984, *Ap. J. (Letters)*, **281**, L25.
- Itoh, H. 1977, *Pub. Astr. Soc. Japan*, **29**, 813.
- Knapp, G. R., Phillips, T. G., Leighton, R. B., Lo, K. Y., Wannier, P. G., Wootten, H. A., and Huggins, P. J. 1982, *Ap. J.*, **252**, 616.
- Mathewson, D. S., Ford, V. L., Dopita, M. A., Touhy, I. R., Long, K. S., and Helfand, D. J. 1983, *Ap. J. Suppl.*, **51**, 345.
- McKee, C. F. 1974, *Ap. J.*, **188**, 335.
- McKee, C. F., and Ostriker, J. P. 1977, *Ap. J.*, **218**, 148.
- Meyer, J. P. 1979, in *Comm. 22e Colloque Internat. d'Ap., Liège, Les Éléments et leurs isotopes dans l'univers*, p. 153.
- Mewe, R., and Gronenschild, E. H. B. M. 1981, *Astr. Ap. Suppl.*, **45**, 11.
- Murray, S. 1984, private communication.
- Murray, S. S., Fabbiano, G., Fabian, A. C., Epstein, A., and Giacconi, R. 1979, *Ap. J. (Letters)*, **234**, L69.
- Oemler, A., and Tinsley, B. M. 1979, *A. J.*, **84**, 985.
- Pisarski, R. L., Helfand, D. J., and Kahn, S. M. 1984, *Ap. J.*, **277**, 710.
- Pravdo, S. H., and Nugent, J. J. 1983, in *IAU Symp. 101, Supernova Remnants and Their X-Ray Emission*, ed. I. J. Danziger and P. Gorenstein (Dordrecht: Reidel), p. 29.
- Pye, J. P., Pounds, K. A., Rolf, D. P., Seward, F. D., Smith, A., and Willingale, R. 1981, *M.N.R.A.S.*, **194**, 569.
- Raymond, J. C., and Smith, B. W. 1977, *Ap. J. Suppl.*, **35**, 419.
- Reid, P. B., Becker, R. H., and Long, K. S. 1982, *Ap. J.*, **261**, 485.
- Richtmyer, R. D., and Morton, K. W. 1967, *Difference Methods for Initial Value Problems* (2d ed.; New York: Interscience).
- Rutishauser, H. 1958, *NBS Appl. Math. Ser., No. 49, Further Contributions to the Solution of Simultaneous Linear Equations and the Determination of Eigenvalues*, p. 47.
- Sedov, L. I. 1959, *Similarity and Dimensional Methods in Mechanics* (New York: Academic Press).
- Seward, F., Gorenstein, P., and Tucker, W. 1983, *Ap. J.*, **266**, 287.
- Shull, J. M. 1982, *Ap. J.*, **262**, 308.
- Szymkowiak, A. 1982, private communication.
- van den Bergh, S., and Kamper, K. W. 1977, *Ap. J.*, **218**, 617.
- Wheeler, J. C. 1980, ed., *Proceedings of the Texas Workshop on Type I Supernovae* (Austin: University of Texas Press).
- White, R. L., and Long, K. S. 1983, *Ap. J.*, **264**, 196.

DAVID J. HELFAND: Columbia Astrophysics Laboratory, Departments of Astronomy and Physics, Columbia University, 538 West 120th St., New York, NY 10027

JOHN P. HUGHES: Harvard-Smithsonian Center for Astrophysics, 60 Garden Street, Cambridge, MA 02138